THEORETICAL AND EXPERIMENTAL INVESTIGATIONS OF A MECHANICAL MODEL FOR ADHESIVELY BONDED PIEZOELECTRIC SENSOR

Naizhi ZHAO[1]

In the realm of structural health monitoring research, the mechanical model of the sensor stands as a pivotal factor, wielding significant impact. This study delves into the piezoelectric (PZT) driving principle inherent to PZT ceramics, thereby establishing a driving vibration model for PZT ceramic sensors based on the tenets of continuous medium dynamics. Through a meticulous exploration of the interaction between the PZT sensor and its bonding layer, the mechanical model's integrity was scrutinized, affirming its feasibility. Furthermore, practical experimentation was undertaken to assess the influence of the model and various adhesive substances on PZT transfer driving force. The findings unequivocally underscore the validity and precision, to a certain degree, of the simplified model proposed herein for bonded PZT drive. The primary focus of this study revolves around examining the structural response under the influence of a bonded PZT sensor, followed by the establishment of a corresponding mechanical model. Special attention is paid to the impact of bonding layer properties on the mechanical model, thereby ensuring that the research outcomes closely align with the sensor's real-world operational conditions, thereby enhancing practicality.

Keywords: PZT sensor; mechanical model; bonded layer; driving force

1. Introduction

In-service pipelines, such as municipal and petrochemical pipelines, undergo inevitable aging during their operational lifespan due to corrosion resulting from chemical reactions or other factors. This gradual deterioration compromises the integrity and load-bearing capacity of the structure, potentially leading to severe consequences. Therefore, it is imperative to explore health monitoring and evaluation technologies for various transportation pipelines to promptly detect pipeline damage and mitigate potential risks[1,2].

Piezoelectric (PZT) materials have emerged as key sensors in large-scale structural health monitoring in recent years, owing to their utilization of the PZT effect. Researchers have shown significant interest in this field. Generally, the integration of PZT with the main structure can be categorized into two types: embedded and bonded sensors. Embedded sensors exhibit polarization in the

[1] Naizhi ZHAO, School of Management Engineering, Jiangsu Urban and Rural Construction Vocational College, China, e-mail: zhaonaizhi@163.com

thickness direction, known as D33 motion, induced by current. In contrast, the polarization direction of bonded sensors differs, with vibration occurring along the length direction, referred to as D31 vibration[3].

The body of literature on PZT applications is extensive, covering a wide range of mechanical theoretical analyses, experimental studies on piezoelectric intelligent structures, vibration control, seismic resilience, structural health monitoring, damage identification technology, active buckling control, and engineering applications. Despite the plethora of research, there remains a dominance of application development and theoretical exploration, with limited numerical simulations and experimental validations. Furthermore, there is a scarcity of in-depth investigations into the coupling and modeling theory between adhesive piezoelectric intelligent drivers and protective layers, hindering the attainment of engineering practicality[4].

This study addresses these gaps by examining the characteristics of PZT drivers, selecting appropriate piezoelectric equations, and developing control equations for the lengthwise vibration of PZT drivers based on continuum dynamics principles. Additionally, the study discusses the material properties of PZT, bonding layer thickness, elastic modulus, and other parameters essential for PZT driver functionality. In conclusion, this research lays a critical theoretical foundation for enhancing the performance of PZT drivers.

2. Theoretical analysis

In the health monitoring of smart structures, a thin-sheet piezoelectric ceramic (PZT) sensor is commonly affixed to the surface of the structure. When subjected to alternating current, the PZT sensor undergoes deformation, primarily elongating in its length direction, and transmits this deformation to the structure in the form of shear force[5,6]. This process is depicted schematically in Fig. 1.

Typically, the PZT sensor is adhered to the surface of the structure being monitored. When subjected to alternating harmonic voltage, the piezoelectric effect induces deformation in the sensor.

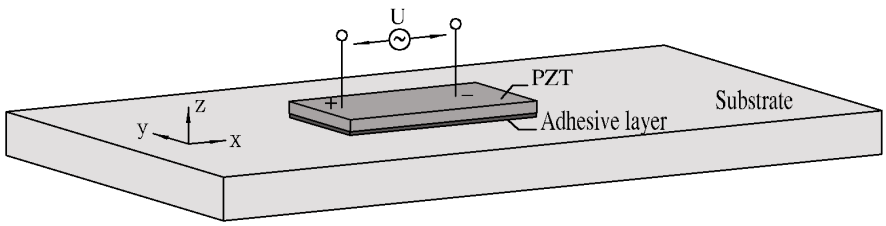

Fig.1. PZT structural diagram

According to Crowley's uniform strain theory, this study operates under the following assumptions [6]:

(1)The bonding layer solely endures shear stress and facilitates load transmission.

(2)The electrodes formed at the top and bottom of the PZT are equipotential.

(3) The driving force generated by the PZT driving sensor only factors in the stress in one direction, specifically the axial normal stress.

(4) The bonding layer shares the same cross-sectional size as the PZT sensor, and the bonding layer is ideal.

(5)The bonding layer shares the same cross-sectional size as the PZT sensor, and the bonding layer is ideal.

2.1 Bonded PZT-driven mechanical model

As illustrated in Fig.2(a), when subjected to alternating harmonic voltage, the sensor adhered to the surface of the structure undergoes deformation primarily along its longer dimension. This deformation is subsequently transmitted to the surface of the structure, effectively introducing an eccentric load in the x-coordinate direction to the detected object, thereby driving the structural response.

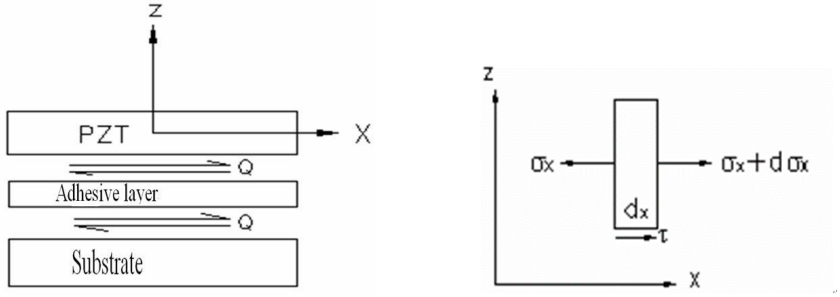

(a) Force conduction diagram of PZT and bonding layer (b) Physical balance conditions

Fig. 2. Bonded PZT sensor works

Building upon the aforementioned theoretical assumptions, incorporating the shear force of the bonding layer and the collaborative deformation of the PZT sensor, the model of the PZT sensor is formulated, yielding the following derivation for the shear force[6,7]:

$$\gamma_j = \frac{V(x,t)}{h_j} \tag{1}$$

The material properties of the bonded layer are as follows:

$$\tau = G_j\gamma_j = G_j\frac{V(x,t)}{h_j} \tag{2}$$

where $V(x,t)$ is the horizontal shear of the adhesive layer; γ_j is the shear strain of the adhesive layer; τ is the stress of the adhesive layer; G_j is the shear modulus of adhesive and $G_j = \frac{E_j}{2(1+v_j)}$; $E_j$is the elastic modulus of adhesive;v_j is layer Poisson's ratio； h_j is the thickness; $E_j.v_j$ are elastic modulus and Poisson's ratio;

As depicted in Fig. 2 (b), we can derive the equation as follows:

$$\rho \frac{\partial^2 V(x,t)}{\partial t^2} = \frac{\partial \sigma_x}{\partial x} + \frac{\tau}{h} \tag{3}$$

According to the second piezoelectric equation, we obtain:

$$\frac{\partial \sigma_x}{\partial x} = c_{11}^E \frac{\partial S_{x1}}{\partial x} \tag{4}$$

Order shows:

$$\rho \frac{\partial^2 V(x,t)}{\partial t^2} = c_{11}^E \frac{\partial^2 V(x,t)}{\partial x^2} + G_j \frac{V(x,t)}{hh_j} \tag{5}$$

That:

$$\frac{\partial^2 V(x,t)}{\partial t^2} - \frac{c_{11}^E}{\rho} \frac{\partial^2 V(x,t)}{\partial x^2} - G_j \frac{V(x,t)}{hh_j} = 0 \tag{6}$$

Where$h$is the piezoelectric ceramic thickness; $\lambda = \sqrt{\frac{c_{11}^E}{\rho}}$is the longitudinal wave velocity which is only related to the material properties of PZT; $\beta = \sqrt{\frac{G_j}{\rho h h_j}}$, is the parameters related to PZT material and bonding layer. $V(x,t)$, λ is defined as$V(x,t) = V_0(x)e^{i\omega t}, \gamma = \sqrt{\frac{\omega^2+\beta^2}{\lambda}} = \sqrt{\frac{\rho h h_j \omega^2 + G_j}{c_{11}^E h h_j}}$, solving the equation (6),can be obtained as:

$$V_0(x) = C_1 cos(\gamma x) + C_2 sin(\gamma x) \tag{7}$$

(In which:(1)$V_0(x)|_{x=0} = 0, C_1 = 0$ (2)$\sigma_x|_{x=\pm\frac{L}{2}} = 0, C_2 = \frac{\Lambda}{\gamma} sec\left(\frac{\gamma L}{2}\right)$.

According to the above conclusions, under the excitation of alternating voltage $U = U_0 sin\omega t$, The displacement equation for the elongated PZT sensor affixed to the structure's surface can be derived as follows:

$$V(x,t) = \frac{\Lambda}{\gamma} sec\left(\frac{\gamma L}{2}\right) sin(\gamma x) sin\omega t \tag{8}$$

The expression for shear stress transfer within the adhesive layer can be derived by considering the material properties and constitutive relation parameters of the adhesive layer[8,9].

$$\tau = G_j \gamma = \frac{G_j sec\left(\frac{\gamma L}{2}\right)}{\gamma h_j} sin(\gamma x) sin\omega t \tag{9}$$

According to Edward F. Crowley's theoretical model, the driving force generated by the sensor acts on both ends of the structure. Consequently, the total shear force exerted on the matrix can be expressed as follows:

$$Q = \frac{G_j \Lambda b}{\gamma^2 h_j} \left[sec\left(\frac{\gamma L}{2}\right) - 1\right] sin\omega \tag{10}$$

The shear force transmitted by the bonding layer is at the coordinates (X, Y) :

$$X = \frac{Lsin\left(\frac{\gamma L}{2}\right) - \gamma L cos\left(\frac{\gamma L}{2}\right)}{4\gamma sin^2\left(\frac{\gamma L}{4}\right)} \text{and } X = \frac{\gamma L cos\left(\frac{\gamma L}{2}\right) - Lsin\left(\frac{\gamma L}{2}\right)}{4\gamma sin^2\left(\frac{\gamma L}{4}\right)}.$$

whereΛ is computes constants, c_{11}^{E} is piezoelectric constants, L is the piezoelectric ceramic longitudinal length.

It can be inferred that the elastic modulus of the bonding layer and the piezoelectric constant of PZT are influential factors affecting the shear force. The deformation induced in the bonding layer by PZT is transferred to the driving force of the matrix. Consequently, a higher modulus of the bonding layer results in a larger DR value [9,10].

2.2 Cantilever deflection calculation

Based on the aforementioned theoretical research, a mathematical model of cantilever beam actuation can be established to validate the rationality of the actuation model. Initially, the driving force generated by the PZT sensor within the structure can be equated to a pair of couples acting on the cantilever beam. Assuming the fixed end as the coordinate origin, with \(x_1 \) and \(x_2 \) denoting the coordinates of the equivalent points, the mechanical model of transverse vibration is depicted in Fig. 3(a), illustrating the force's effect on the micro-segment as shown in Fig. 3(b) below[11,12].

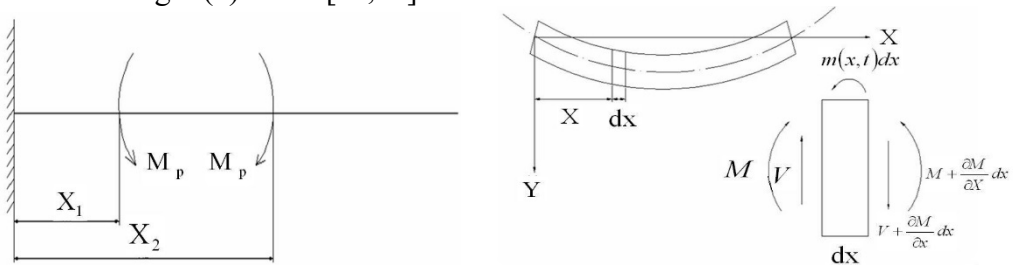

(a) The forces of structure (b) The forces of role in the micro segment

Fig.3.Mechanical model of transverse vibration

The initial position is in a stationary state. Assuming that the equation is $y(x,t) = 0$, the cantilever beam begins to vibrate under the excitation of the driving force generated by PZT. The micro-element is taken for analysis. At a certain time point (x,t), the equation is $m(x,t)dx, M_P(x,t) = Q(x,t)\frac{h_b}{2}$.

Based on the equilibrium condition of the micro-segment force depicted in Fig. 3(a)(b):

$$\rho_b A_b \frac{\partial^2 w}{\partial t^2} dx = \frac{\partial V}{\partial x} dx \tag{11}$$

$$V dx = \frac{\partial M}{\partial x} dx + m dx \tag{12}$$

We have:

$$\rho_b A_b \frac{\partial^2 w}{\partial t^2} = \frac{\partial V}{\partial x} \tag{13}$$

$$V = \frac{\partial M}{\partial x} + \frac{\partial M}{\partial x} \tag{14}$$

Through the incorporation of the ideal Euler beam model, the ensuing relationship can be derived:

$$M = -E_b I_b \frac{\partial^2 w}{\partial x^2} \tag{15}$$

where $M_P(x,t)$ is generate torque, h_b is the cantilever beam height; A_b cantilever beam cross-sectional area; ρ_b is the cantilever beam density; $E_b$is the elastic modulus of cantilever, $I_b = \frac{b_b(2h_b)^3}{12}$is Moment of inertia of beam cross-section of the Y axis; the thickness of the beam is$2h_b$.

Substituting Eq. (15) into eq. (14), we can get:

$$V = \frac{\partial}{\partial x}\left(-E_b I_b \frac{\partial^2 w}{\partial x^2}\right) + \frac{\partial m}{\partial x} \tag{16}$$

So, we can get:

$$\rho_b A_b \frac{\partial^2 w}{\partial t^2} = \frac{\partial^2}{\partial x^2}\left(-E_b I_b \frac{\partial^2 w}{\partial x^2}\right) + \frac{\partial^2 m}{\partial x^2} \tag{17}$$

$$\frac{\partial^2}{\partial x^2}\left(E_b I_b \frac{\partial^2 w}{\partial x^2}\right) + \rho_b A_b \frac{\partial^2 w}{\partial t^2} = \frac{\partial^2 m}{\partial x^2} \tag{18}$$

The lateral vibration differential Equation (18) delineates the behavior of a cantilever beam subjected to the effects of a PZT driver. Through the utilization of the expansion theorem of natural modes, it becomes viable to express the deflection as a linear combination[13].

$$w(x,t) = \sum_{i=1}^{n} \Phi_i(x)\, q_i(t) = \Phi q \tag{19}$$

$\Phi = [\Phi_1(x) \cdots \Phi_n(x)]$ is the normalized mass matrix;

$q = [q_1(t) \cdots q_n(t)]^T$ is coordinate vector;

So we can get the Eq. (20):

$$w = w(L_b, t) = \sum_{i=1}^{n} \Phi_i(L_b)\, q_i(t) = \Phi_L q \tag{20}$$

where L_b is cantilever length.

The second and fourth-order partial derivatives of t and x are calculated respectively. The results are brought into Eq. (19), a new Eq. (21) can be get:

$$E_b I_b \sum_{i=1}^{n} \frac{d^4 \Phi_i}{dx^4} q_i + \rho_b A_b \sum_{i=1}^{n} \frac{d^2 q_i}{dt^2} \Phi_i = P_n \tag{21}$$

We have:

$$M_n \ddot{q}_n(t) + \omega_n^2 M_n q_n(t) = P_n \tag{22}$$

For the cantilever structure:

$$\Phi_n(x) = sin\left[\left(\frac{2n-1}{2l}\pi\right)x\right], \omega_n = \left[\frac{(2n-1)\pi}{2}\right]^2 \sqrt{\frac{EI}{ml^4}} \quad ,n = 1,2\cdots$$

The outcomes of the calculations for generalized mass and generalized load are presented below:

$$M_n = \int_0^l \Phi_n(x)^2 m(x) dx = \bar{m} \int_0^l sin^2\left(\frac{2n-1}{2l}\pi x\right) dx = \frac{\bar{m}l}{2} \tag{23}$$

$$M_n = \int_0^l \Phi_n(x) \frac{\partial^2 m(x,t)}{\partial x^2} dx = \int_{x_1}^{x_2} \Phi_n(x) \frac{\partial^2 m(x,t)}{\partial x^2} dx = a_n M_P \tag{24}$$

where $a_n = \left[\Phi_n''(x_2) - \Phi_n'(x_2) - \Phi_n''(x_1) + \Phi_n'(x_1)\right]$eq. (22) of the Duhamel integral solution is：

$$q_n(t) = \frac{1}{M_n\omega_n}\int_0^t P_n(\tau)\, sin\, \omega_n(t-\tau)\, d\tau \tag{25}$$

Substituting the parameters M_n, P_n, q_n into Eq. (20), then into eq. (22), a new equation of the deflection of the cantilever beam under the action of equal can be derived[14].

3. Experimental Study

The experiment is divided into two phases: initially, the driven model of flexible structures is validated. In this phase, PZT is affixed to the surface of the structure, with the PZT ceramics being driven by PZT driving power. The driving force then traverses through the bonding layer to induce structural vibration. Subsequently, the influence of the layer on the PZT driving force is examined. By selecting different binders and transmitting the same signal, the effects on the free end displacement of the cantilever structure at its first and second natural frequencies are tested and compared. Furthermore, variations in the PZT sensor signal are analyzed to elucidate the impact of the adhesive force of the PZT driver.

3.1 Cantilever Beam Modal Analysis

When the PZT sensor imparts motion to a flexible structure, such as a cantilever aluminum beam, and the frequency of the transmitted signal matches the natural frequency of the structure, resonance occurs, resulting in optimal drive performance. The theoretical calculation of the first natural frequency of the cantilever is essential for understanding this phenomenon. This calculation focuses solely on the plane bending vibration of the beam, excluding the effects of moment of inertia and shear force-induced deformation.

When analyzing the plane bending vibration of a beam, it is customary to exclude the influence of moment of inertia and shear force-induced deformation. This allows us to derive a simplified differential equation that accurately represents the bending behavior of the beam [14,15]. The resulting equation governing the beam's bending vibration is as follows:

$$\frac{\partial^2}{\partial x^2}\left[EI(x)\frac{\partial^2 w(x,t)}{\partial x^2}\right] = -m(x)\frac{\partial^2 w(x,t)}{\partial t^2} \tag{26}$$

According to the boundary conditions:

(1)$x = 0, w(0,t) = 0, \left.\frac{\partial^2 w(x,t)}{\partial x}\right|_{x=0} = 0$;

(2)$x = l, EI(x)\left.\frac{\partial^2 w(x,t)}{\partial x^2}\right|_{x=0} = 0, \frac{\partial}{\partial x}\left[EI(x)\frac{\partial^2 w(x,t)}{\partial x^2}\right]\Big|_{x=l} = 0.$

Applying $w(x,t) = W(x)W(t)$,then $w(x,t) = W(x)\sin\omega t + \phi$,we can get：

$$w(x) = C_1 \sin\beta x + C_2 \cos\beta x + C_3 \sin h\beta x + C_4 \cos h\beta x \quad (27)$$

Substituting the boundary conditions into the formula we can get：

$$\omega_{ni} = \left(\frac{(2i-1)\pi}{2l}\right)^2 \sqrt{\frac{E_b I_b}{\rho_b A_b}} (i = 1,2,3\cdots) \quad (28)$$

Where $w(x,t)$ is the deflection displacement variable; $W(x)$ is the deflection coordinate variable; $W(t)$is the deflection time variable.

In general, the vibration energy of a cantilever beam in higher modes is typically minimal. Even if higher modes of vibration occur in the free state, their presence tends to decay rapidly. The majority of vibration energy is concentrated in the lower order modes. Therefore, it is common practice to focus on the first three vibration modes when analyzing a cantilever beam [14,15].

In the experimental procedure, the beam was subjected to a swept sine wave ranging from 1 to 100 Hz via the excitation system. Subsequently, spectral analysis was conducted using MATLAB software to ascertain the first three natural frequencies of the beam. This methodology adheres to established practices in structural dynamics analysis, facilitating accurate determination of the beam's vibrational characteristics.

Table 1 presents the initial three natural frequencies of the cantilever beam based on theoretical calculations, juxtaposed with the corresponding experimental results. A comparison between the theoretical and experimental values indicates a high level of consistency, affirming the accuracy of the data obtained through experimentation. This alignment underscores the reliability of the theoretical predictions in modeling the dynamic behavior of the cantilever beam.

Table 1

The natural frequency of cantilever

	First order natural frequency /Hz	Second order natural frequency /Hz	Third order natural frequency /Hz
Experimental value	1.54	9.35	25.30
Theoretical value	1.64	9.77	26.85

3.1.1 Experimental Test Setup

The experimental setup comprises a signal transmitter, a power amplifier, a PZT sensor, and a signal receiver. A self-generated sine five-peak wave digital signal is inputted by the signal generator. This digital signal, transmitted through

the PZT sensor, generates a driving force to excite the cantilever beam. The power amplifier amplifies the signal power by a factor of 15, thereby enhancing the driving force applied to the cantilever beam structure to mimic the theoretical driving model[16,17].

For this experiment, the laser displacement sensor utilized is the ft50220 model produced by Beijing FeiTuo Cinda Laser Technology Co.LTD. This displacement sensor features an effective range of 80 mm to 300 mm and boasts an accuracy of 0.01 mm.

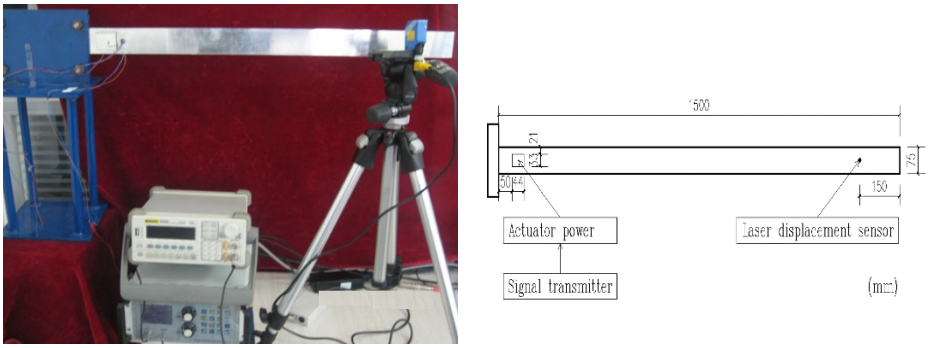

(a)Test system (b) Schematic diagram

Fig.4. Test system and schematic diagram

Fig. 4 illustrates the principle and testing system. Utilizing a non-contact displacement meter ensures that the fundamental frequency structure remains unchanged, thereby mitigating errors associated with contact measurements and yielding more precise test outcomes. The experimental setup involves a 1 mm thick flexible aluminum cantilever beam, with the driving element being PZT-4, sized at 44 × 33 × 1 mm. The laser displacement sensor's light spot is positioned at a distance of 150mm from the central axis of the cantilever's free end.

The experimental parameters are delineated as follows: the sinusoidal excitation signal is generated by the PZT sensor. The excitation signal is comprised of a 5-peak wave signal modulated by the Hanning window function. Specifically, the frequencies employed are 1.54 Hz and 9.35 Hz, while the voltage amplitude ranges from 75 to 300 V.

3.1.2 Experimental result

In this experiment, the first two natural frequencies of the beam serve as the excitation signal frequencies, with the PZT sensor employed to transmit the signal within the voltage range of 75 V to 300 V. Subsequently, based on the experimental data, the amplitude of the displacement curve of the free end of the beam is depicted (refer to Fig. 5).

Under the excitation of the first-order frequency, the displacement of the free end measures 2.732 mm, representing a deviation of 17.58% from the theoretical calculation. Similarly, at the second-order frequency, the observed deviation stands at 17.61%.

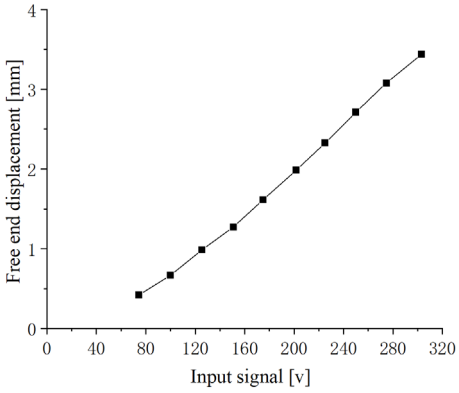

(a) First resonance

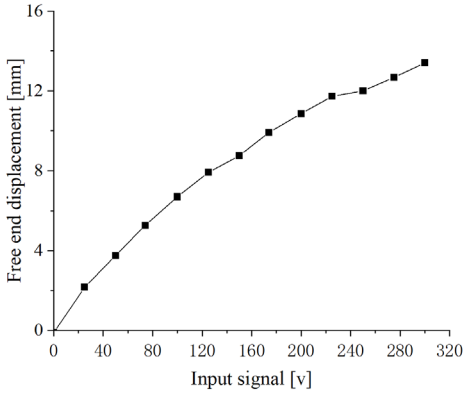

(b) Second resonance

Fig.5.The relationship between resonance and input voltage

The accuracy of the bonded PZT drive model can be assessed by comparing experimental data with theoretical predictions. While there is inevitably some margin of error, the overall accuracy generally aligns with theoretical expectations. This discrepancy can often be attributed to simplifications and assumptions made in the modeling process. Additionally, variations in material properties and experimental conditions can also impact the accuracy of the results. In summary, the conservative approach to expressing these findings in academic writing underscores the need to acknowledge and address potential sources of error in the analysis[18].

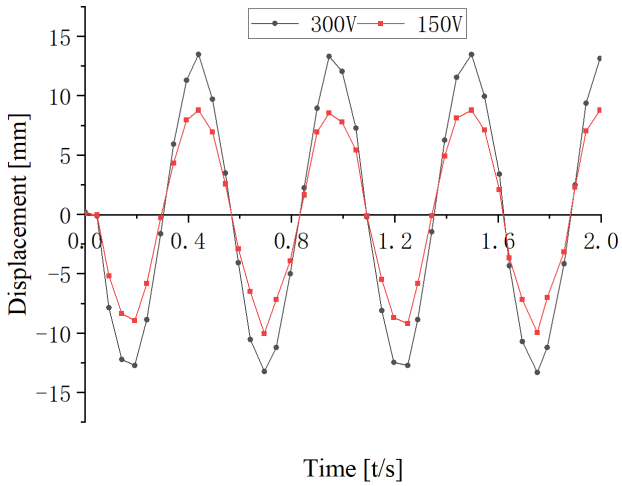

Fig.6. Displacement curves under different input voltages

Based on the calculated data, the first-order resonance curve depicting the displacement of the free end of the arm beam (refer to Fig. 6) has been generated. From the analysis, it can be inferred that the displacement of the free end of the beam exhibits a proportional increase in response to the driving force generated by the applied voltage. Furthermore, the observed trend indicates that the displacement of the free end also experiences a concurrent increase. This observation underscores the relationship between the applied voltage and the resulting displacement, highlighting the importance of understanding the dynamic response of the system under varying driving forces.

3.2 Experimental of the impact of the layer for the PZT driving force

3.2.1 Experimental setup

The experimental system diagram is shown in Fig. 7. The signal is transmitted from an arbitrary waveform generator (RIGOL DG10x2), which emits a modulated sine ultrasonic guided wave signal using a Hann window function. After being amplified by an amplifier (ATA-1220E), the guided wave signal is input to a PZT actuator. The PZT actuator generates driving force through the piezoelectric effect, causing guided waves to propagate within the aluminum plate. The PZT sensor receives the guided wave signal in the aluminum plate and transmits it to an oscilloscope (RIGOL DSl000E), forming a digital signal. By processing the signal, the mechanical model of the bonded PZT actuator can be determined, as well as the effects of different adhesives on the shear force transmitted during PZT actuation. This enables the identification of an optimal actuator arrangement, laying the foundation for future structural health monitoring [18,19].

Two types of tests were conducted to validate the performance of the PZT attachment methods. The PZT was affixed to the structure surfaces using different binders with employing 502 glue and utilizing AB glue.

The first test involved analyzing the PZT sensor signals using an oscilloscope, as outlined in Fig.8. By comparing these sensor signals, the influence of different bonding layers on the PZT driver's performance was assessed.

Subsequently, the second test focused on evaluating the impact of the first natural frequency on the displacement of the free end. This verification process aimed to ensure consistency with the model validation test, thereby validating the accuracy of the experimental setup and results.

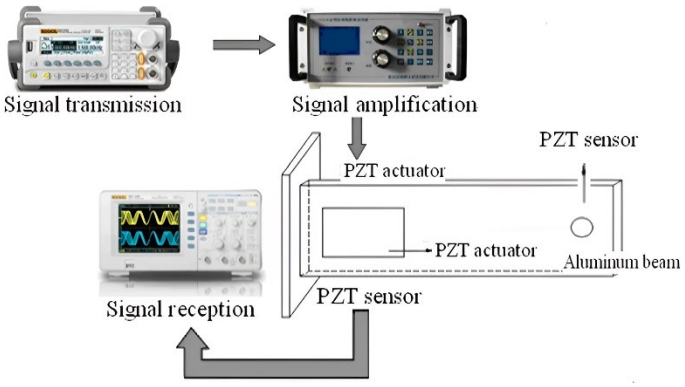

Fig.7. Experimental schematic diagram

3.2.2 Experimental result and discussion

Upon analysis of the test data, it was observed that under the first-order frequency, PZT bonding with the matrix structure using different adhesives resulted in varying input signals and PZT sensor responses, as depicted in Fig. 8 (a). Similarly, under the second frequency, the relationship between the signals is illustrated in Fig. 8 (b).

To further investigate, the displacement was measured and compared. For the first-order frequency signal input of 300 V, the resulting displacement curves of the cantilever's free end, bonded with different layers, are presented in Fig. 9. These curves offer insight into the impact of adhesive choice on the dynamic response of the system, providing valuable information for further analysis and optimization [20-22].

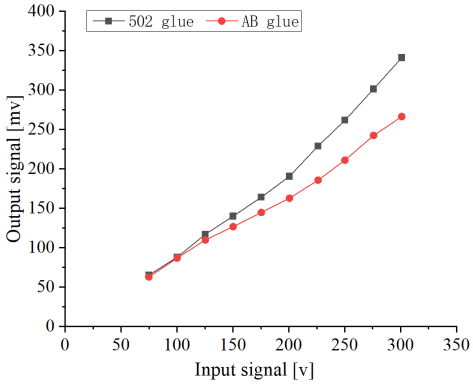

(a) 1st vibration modes excitation

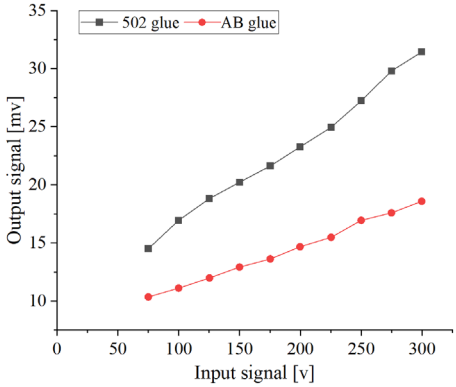

(b) 2nd vibration modes excitation

Fig.8.The relationship between driving signal and sensor signal

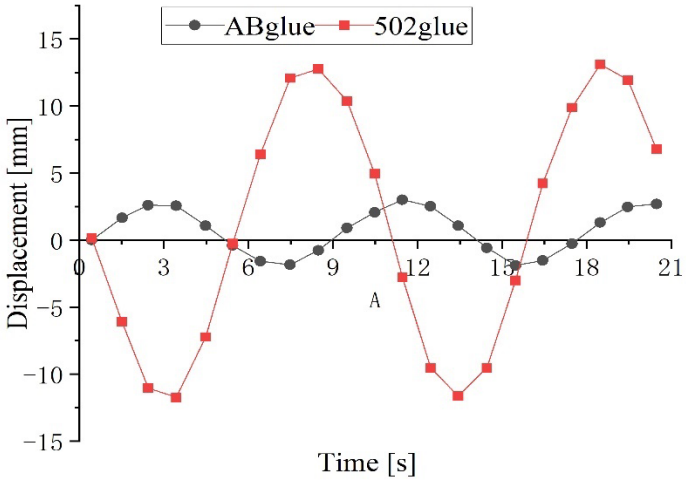

Fig.9.1st vibration modes frequency of the structure under the free end of different adhesive layer displacement curves

The results of the two experiments reveal a significant trend: a thicker bonding layer corresponds to a reduced transfer of the PZT driver. This phenomenon can be attributed to the smaller elastic modulus of the bonding layer, resulting in diminished delivery of the PZT driving force. The increased thickness of the bonding layer leads to greater deformation and absorption of the driving force generated by the PZT. Consequently, when the electrical signal is transmitted from the PZT to the structure, the driving force is attenuated.

To fully harness the driving capabilities of the PZT, it is imperative to make a judicious selection regarding the type and thickness of the bonding layer. This ensures optimal performance by mitigating the effects of excessive absorption and deformation.

Furthermore, it is noteworthy that these experimental findings align qualitatively with theoretical expectations. This consistency reinforces the validity and reliability of the experimental methodology and underscores the importance of informed material selection in optimizing PZT-driven systems.

4. Conclusions

The primary objective of this paper is to develop a mechanical model for bonded PZT sensors. Drawing upon theoretical insights into the second type of PZT-electric couple and continuum dynamics, the mechanical model is constructed while accounting for the interaction between the PZT and the structural matrix.

Validation and rationalization of the simplified mechanical model of the bonded PZT driver are achieved through theoretical analysis and illustrative examples. This process enhances the fidelity of the model, bringing it closer to real-world scenarios. The findings affirm that the interaction between the PZT and the bonded structural layer constitutes the primary determinant of the mechanical model.

By establishing this model and corroborating its validity, this research contributes to a deeper understanding of PZT-driven systems and facilitates their optimization for various applications.

In the mathematical model of the actuator established under free boundary conditions by Tzou in references 1, 2, and 3, along with the expression for control force derived by Ghaedi using the principle of virtual work, Padma developed a piezoelectric driving model attached to a cantilever beam based on the driving force of the piezoelectric actuator and the applied electric potential. This model offers several advantages over previous models. The research primarily focused on the effects of the bonding layer between the PZT and the structure during the modeling process, enabling a more realistic theoretical model of PZT driving. Under various frequency excitations, the experimental displacement deflection at the free end of

the cantilever structure was compared with theoretical values, revealing a small error and a close approximation to actual working conditions.

REFERENCES

[1]. *O. Avci, O. Abdeljaber, S. Kiranyaz, et al.,* A review of vibration-based damage detection in civil structures: From traditional methods to machine learning and deep learning applications, Mech. Syst. Signal Process. **vol.**147 ,2021, pp. 107077

[2]. *C. Du, S. Dutta, P. Kurup, et al.,* A review of railway infrastructure monitoring using fiber optic sensors, Sensors A Phys., **vol.**303 ,2020, pp. 111728

[3]. *Wongi S. Na,* Possibility of detecting wall thickness loss using a PZT based structural health monitoring method for metal based pipeline facilities, NDT & E International, 2017

[4]. *GHAEDI S K, MISRA A K.,* Active control of shallow spherical shells using piezoceramic sheets, Smart Structures and Materials: Smart Structures and Integrated Systems, 1999, pp. 890-912

[5]. *Lee C K.,* Theory of laminated piezoelectric plates for the design of distributed sensors/actuators. Part I: Governing equations and reciprocal relationships, Acoustical Society of America. **vol. 87**, no. 3, 1990, pp. 1144-1158

[6]. *Tong L, Sun D, Atluri S N.* Sensing and actuating behaviours of piezoelectric layers with debonding in smart beams. Smart Materials & Structures, **vol. 10**, no. 4, 2001, pp. 713

[7]. *Campbell J F, Vanderheiden E G, Martinez L A,* et al., A Multi-Purpose Sensor for Composite Laminates Based on a Piezo-Electric Film, Journal of Composite Materials. **vol. 26**, no. 3, 2006, pp. 334-349

[8]. *Yanyu M, Shi Y, Xiaolong W.*, Mechanical modeling and experimental validation on piezoceramic based on the surface-bonded PZT sensor, Surface Review and Letters, **Vol. 26**, No. 06, 2019, pp. 1850209

[9]. *Zhao Naizhi, Chen Guifeng,* The studies of a mechanical model for adhesively bonded PZT sensor, 2017 3rd IEEE International Conference on Control Science and Systems Engineering (ICCSSE), 2017

[10]. *Zhao, Nai Zhi, Shi Yan, Chang Tie Huang*, The Theoretical Study of a Mechanical Model for Bonded PZT Sensor, Applied Mechanicsand Materials, 2011

[11]. *Tzou H S, Bao Y, Venkayya V B,* Parametric Study of Segmented Transducers Laminated on Cylindrical Shells, Part 2: Actuator Patches J. Journal of Sound & Vibration. **vol. 197**, no. 2, 1996, pp. 207-224

[12] *Belotserkovskiy P M,* ON THE OSCILLATIONS OF INFINITE PERIODIC BEAMS SUBJECTED TO A MOVING CONCENTRATED FORCE, Journal of Sound & Vibration, **vol.**193, no. 3, 1996, pp. 705-712

[13]. *Jafari M, Fesharaki J J.*, Buckling Analysis of Cylinders Reinforced with Stiffening Rings and Foam, Numerical and Experimental Investigation, Strength of Materials, **vol. 53**, 2021, Jun

[14]. *Alam M, Mishra S K.*, Postcritical Imperfection Sensitivity of Functionally Graded Piezoelectric Cylindrical Nanoshells Using Boundary Layer Solution, Journal of Engineering Mechanics, **vol. 149**, no. 9, 2023, pp. 4023055-1-4023055-19.

[15]. *Qiu Han, Fan Mu, Deng Yan, et al.*, Dynamic Analysis of Flexoelectric Actuated Truncated Conical, Shells AIAA Journal, **vol. 61**, no. 11, 2023, pp. 5061-5075

[16]. *Raju J, Bhalla S, Visalakshi T.,* Pipeline corrosion assessment using piezo-sensors in reusable non-bonded configuration, NDT & E International, **vol. 111**, 2020, pp. 102220

[17]. *Wen-Chao Sui, Yong-Chen Pei, Si-Jia Liu, et al.*, A Self-Sensing Interwoven Network With Superelastic SMA Wires, IEEE Transactions on Industrial Electronics, 2023

[18]. *Gonzalez-Jimenez A, Lomazzi L, Junges R, et al.,* Enhancing Lamb wave-based damage diagnosis in composite materials using a pseudo-damage boosted convolutional neural network approach, Structural Health Monitoring, **vol. 23**, no.3, 2024, pp. 1514-1529.

[19]. *Ai D, Cheng J.*, A deep learning approach for electromechanical impedance based concrete structural damage quantification using two-dimensional convolutional neural network, Mechanical Systems & Signal Processing, **Vol. 183**, No. 15, 2023, pp. 109634

[20]. *Jia J, Zheng X, Guo S, et al.,* Removing Stripe Noise Based on Improved Statistics for Hyperspectral Images, IEEE Geoscience and Remote Sensing Letters, **Vol. 99**, 2020, pp. 1-5

[21]. *Hong H P,* An efficient point estimate method for probabilistic analysis, Reliability Engineering & System Safety, **vol. 59**, no. 3, 2020, pp. 261-267

[22]. *Zhang X, Xu J, Yan R,* A structural impedance measurement method by using polyvinylidene fluoride as actuator and sensor, Review of Scientific Instruments, **vol. 91**, no. 91, 2020, pp. 085-111